nature communications

Article

https://doi.org/10.1038/s41467-026-69440-x

Millimeter-wave dielectric tunability driven by topological polar structure switching in $PbTiO_3/SrTiO_3$ superlattices

Received: 10 March 2025

Accepted: 30 January 2026

Published online: 13 February 2026

Check for updates

Sixu Wang[1,7], Jiyuan Yang[2,7], Hanbin Gao[3,7], Kazuki Okamoto[4,7], Rui Liu[5], Yunpeng Ma[1], Tao Zhou[5], Martin Holt[5], Qiang Zheng[3], Hiroshi Funakubo[4], Shi Liu[2,6] ✉, Jing-Feng Li[1] & Qian Li[1] ✉

Dielectric tunability induced by an external electric field in materials underpins radio frequency signal modulation devices such as phase shifters, which are critical components in wireless communication and sensing systems. However, the tunability and integrability of current devices have yet to be enhanced for emerging applications, particularly at millimeter-wave frequencies. Here, we demonstrate that topological polar structures formed in $PbTiO_3/SrTiO_3$ superlattices exhibit large tunable in-plane dielectric properties, as determined by their multiscale structural configurations and polarization switching behaviors. Under a moderate field of 30 kV cm^{-1}, the dipole wave structure maintains a tunability exceeding 15% at 70 GHz and above 8% over the measured range up to 110 GHz, contrasting with the weakly tunable flux closure structure. Based on in situ structural characterizations and molecular dynamics simulations, we delineate the polarization switching processes and elucidate the mechanisms underlying the observed tunable millimeter-wave dielectric responses. Our results provide new insights into the high-frequency dielectric properties of topological polar phases, potentially broadening the versatility of these materials in next-generation integrated electronic applications.

Topological polar structures have attracted considerable attention in recent years because of their unique swirling polarization configurations and topological protection mechanisms that distinguish them from conventional ferroelectric materials[1]. The established topological polar structures are exemplified by polar vortices, skyrmions, and merons[2–7] formed in $PbTiO_3/SrTiO_3$ superlattices and multilayers, which have been extensively investigated through microscopic observations and simulations. Aside from these structures, dipole waves exhibit a continuous head-to-tail arrangement of electric dipoles along in-plane directions as opposed to separate vortex units[8], forming a sinusoidal polarization distribution profile with an in-plane modulation periodicity. Flux closures, by contrast, are characterized by domains with alternating in-plane or out-of-plane polarization vectors, separated by 90° and 180° domain walls[9]. These domain walls act as sharp edges between areas with different polarization directions and inhomogeneous lattice strains. The formation of these different

[1]State Key Laboratory of New Ceramic Materials, School of Materials Science and Engineering, Tsinghua University, Beijing, China. [2]Department of Physics, School of Science and Research Center for Industries of the Future, Westlake University, Hangzhou, Zhejiang, China. [3]CAS Key Laboratory of Standardization and Measurement for Nanotechnology, National Center for Nanoscience and Technology, Beijing, China. [4]School of Materials Science and Engineering, Institute of Science Tokyo, Yokohama, Kanagawa, Japan. [5]Center for Nanoscale Materials, Argonne National Laboratory, Lemont, IL, USA. [6]Institute of Natural Sciences, Westlake Institute for Advanced Study, Hangzhou, Zhejiang, China. [7]These authors contributed equally: Sixu Wang, Jiyuan Yang, Hanbin Gao, Kazuki Okamoto. ✉e-mail: liushi@westlake.edu.cn; qianli_mse@tsinghua.edu.cn

types of topological structures primarily arises from the electrostatic screening and elastic effects within the superlattices, involving a delicate balance of competing free energy components related to the polarization and strain states[10,11]. Therefore, their phase stabilities can be engineered by tuning the relative thickness of the component layers[8,12–14].

The characteristic polarization topology of these structures leads to a distinct response to electric fields at different frequencies. Previous studies have mostly investigated their polarization evolution behaviors under the influence of low-frequency electric fields[15,16], showing characteristic switching processes[17,18] and anomalous dielectric responses such as negative permittivity[19,20,21] linked to topological protection behaviors. Meanwhile, the dynamic response of these structures have also been explored in the higher frequency range (from terahertz to optical frequencies), revealing ultrafast collective dynamics and nonequilibrium phase transitions of polar vorties[22–25]. Exploring the polarization dynamics within the microwave to millimeter-wave bands (1–300 GHz) could bridge the gap between the low-frequency and subterahertz ranges and unlock novel electronic properties of topological polar structures at these frequencies. Notably, the dipole wave and flux closure structures may potentially exhibit complex in-plane polarization dynamics due to the existence of net in-plane polarization at the static states.

Meanwhile, the rapid development of next-generation wireless communications and sensing technologies has driven the demands for high-performance millimeter-wave tunable dielectrics[26]. These applications, including frequency-agile filters, adaptive phase shifters, and phased array antennas, hinge on efficient electric-field tuning of the dielectric permittivity of working materials. Ferroelectrics exhibit tunable dielectric properties, as observed in various material systems such as (Ba,Sr)TiO_3, Pb(Zr,Ti)O_3, and (K,Na)NbO_3[27–32], which have advantages over semiconductors and other types of materials in terms of tunable high permittivity, large bandwidth and low loss[33]. While ferroelectric-based tunable devices were demonstrated at microwave frequencies[27,34–38], few studies have extended the operating frequency to millimeter-wave bands (over 40 GHz) thus far. To address this, explorations into millimeter-wave polarization dynamics and associated dielectric tuning mechanisms becomes pivotal for extending functionalities of ferroelectrics into high-frequency regimes.

Here, we demonstrate large in-plane dielectric tunability at millimeter-wave frequencies in $PbTiO_3$/$SrTiO_3$ superlattices hosting dipole waves and flux closures. By systematically adjusting the thickness of $PbTiO_3$ layers, the superlattices exhibit varying topological phase stabilities, leading to distinct polarization switching dynamics and tunable dielectric responses. Our results not only reveal the polarization evolution mechanisms of topological polar structures under electric fields extending into the millimeter-wave range, but also establish these systems as a promising material platform for tunable millimeter-wave device applications.

Results

Superlattice growth and structural characterization

We select a series of $(PbTiO_3)_n/(SrTiO_3)_8$ superlattices with $n = 12$, 15, 20, and 22, and total thicknesses ranging from ~165 nm to ~183 nm (see details in Supplementary Table 1), as representative systems hosting topological polar phases. All the superlattices were epitaxially grown on (001)-cut $(LaAlO_3)_{0.3}$-$(SrAl_{0.5}Ta_{0.5}O_3)_{0.7}$ (LSAT) single crystal substrates buffered with a 5 nm $GdScO_3$ buffer layer. The $GdScO_3$ layer introduces a relaxation of the lattice mismatch strain so that the average in-plane lattice constants are determined to be ~3.93 Å from X-ray diffraction (XRD) measurements. Coupled $2\theta/\omega$-scans across the LSAT 002 reflection (Supplementary Fig. 1a) exhibit well-defined superlattice peak fringes, indicating their excellent crystallinity and clear interfaces as a result of high-quality film growth. The out-of-plane layer periodicities of the superlattices are extracted to be ~8.0–11.8 nm from the fringes, which agrees with the designed values. The average out-of-plane lattice constant c of the superlattices can be calculated from the positions of the zeroth-order superlattice peak ($SL_{(0)}$, marked in Supplementary Fig. 1a). As shown in Fig. 1c, the lattice constant c increases with increasing $PbTiO_3$ layer thickness n, suggesting a concomitant increase in the out-of-plane polarization component in the $PbTiO_3$ layers.

X-ray reciprocal space mapping (RSM) about the LSAT 103 reflection (Fig. 1a) shows diffraction intensities of second- and even third-order satellites separated from the superlattice peaks along the Q_x/Q_y directions, in contrast to only the first-order diffraction satellites in previously observed polar vortices or skyrmions[2,4,16,22]. This indicates the existence of topological phases with strong in-plane ordering in these superlattices. As the $PbTiO_3$ layer thickness n decreases from 22 to 12, the satellite peaks shift further from the superlattice peaks, suggesting smaller in-plane periodicities (Fig. 1b). The calculated in-plane periodicity d ranges from approximately 9.1 nm to 13.6 nm, and increases with n in a nearly linear manner (Fig. 1c). This trend fits well with the scaling equation d (nm) = $2.015 + 13.46/n + 0.497n$, in agreement with previous studies[39]. The satellites also split into fringes along the Q_z direction with the same Q_z values as the superlattice peaks, evidencing an out-of-plane ordering with the same superlattice periodicities. As the diffraction satellites originate from topological phases in the $PbTiO_3$ layers, such ordering states imply strong interlayer polarization coupling across different $PbTiO_3$ layers. Similar interlayer coupling has been observed in vortex-hosting $(PbTiO_3)_n/(SrTiO_3)_m$ superlattices with thicker $PbTiO_3$ layers than $SrTiO_3$ layers[12,13], as is the case here ($n = 12$ ~ 22, $m = 8$). The existence of both in-plane periodicity and out-of-plane interlayer coupling renders our superlattices a model ordered system for investigating the structural evolution and dielectric properties of topological polar phases. Notably, the 002 RSM for the $n = 12$ superlattice shows diffraction intensities apart from the superlattice peaks (see the box-marked region in Supplementary Fig. 1b), which are attributed to tilted ferroelectric a-domains similar to those of single-layer $PbTiO_3$ films with c/a domain structures[40].

Nanobeam X-ray diffraction imaging further reveals the mesoscopic spatial distribution of different topological phases in the superlattices[41,42]. For the $n = 12$ superlattice, mapping of the tilted a-domain diffraction intensities within a slice of reciprocal space around the 002 reflection (see the boxed region in Fig. 1d) reveals uniformly distributed stripes with high diffraction intensities (Fig. 1e). The observed diffraction contrast indicates the locations of tilted a-domains, occupying approximately 40% of the mapped area (see Supplementary Note 3 and Supplementary Fig. 8). Such coexistence of topological polar structures and conventional a-domains has also been reported in polar vortices[15]. Although similar diffraction peaks are also observed in the $n = 15$ superlattice, their intensities are significantly weaker than those in the $n = 12$ superlattice, along with smaller full widths at the half maximum (Supplementary Fig. 1b, c). The spatial distribution of such diffraction intensities is more concentrated along with a smaller area proportion of ~12%, which is more likely associated with dislocations in the films, as shown in Fig. 1f, g.

High-angle annular dark-field scanning transmission electron microscopy (HAADF-STEM) reveals the real-space polarization configurations of the topological phases, as presented in Fig. 1h–j. Large field-of-view images of the superlattices confirm the microstructures of the uniform $PbTiO_3$ and $SrTiO_3$ layers with sharp interfaces, as well as their designed layer thicknesses (Fig. 1h). The maps of polar displacement vector (arrows in Fig. 1i, j), derived from the cation column positions in the atomically resolved HAADF images, show varying polarization configurations in the superlattices. Figure 1i, j presents

https://doi.org/10.1038/s41467-026-69440-x

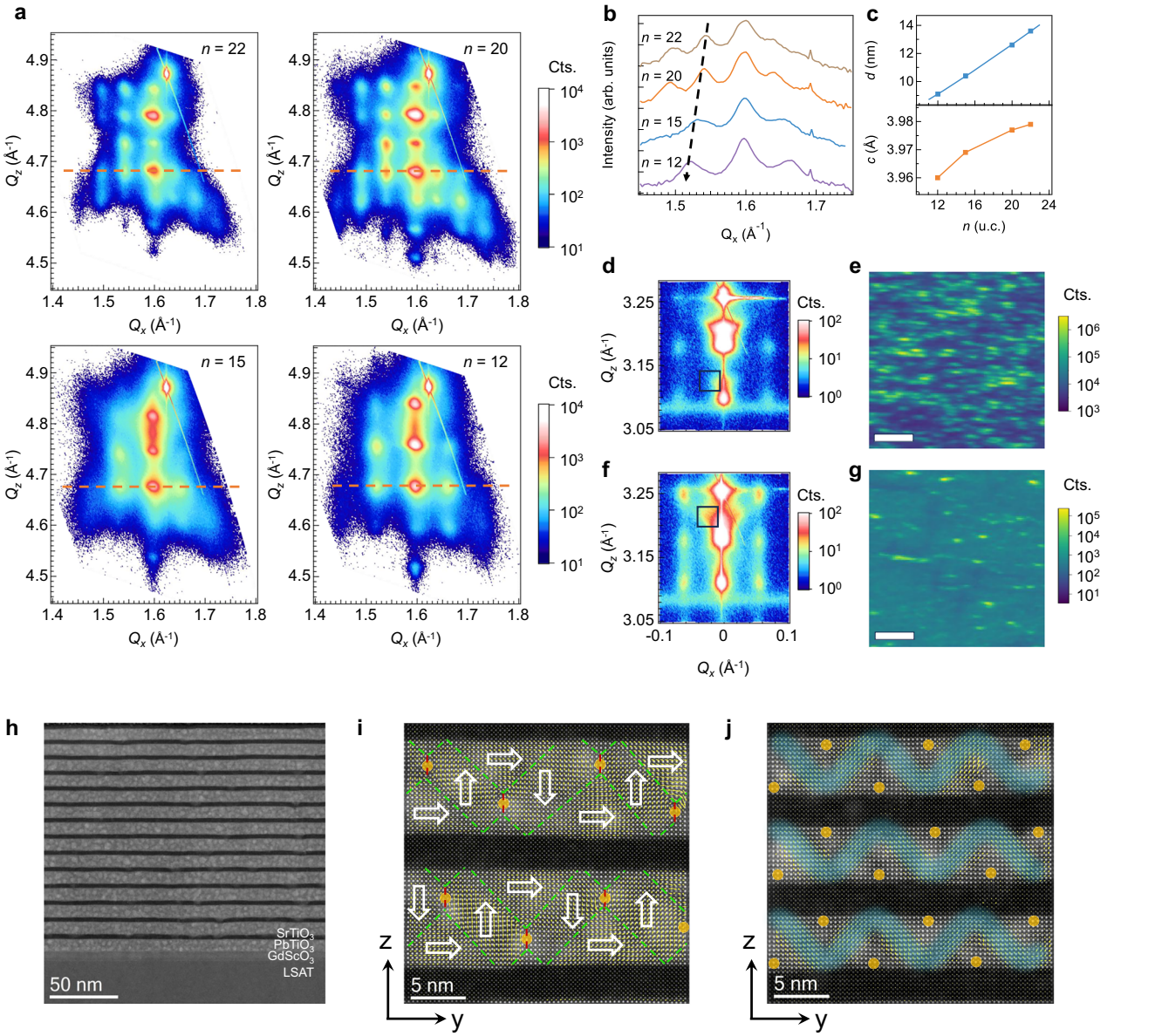

Fig. 1 | Structural characterizations of $(PbTiO_3)_n/(SrTiO_3)_8$ superlattices. a *H0L*-slice (at $Q_y = 0$ Å^{-1}) X-ray RSM around LSAT 103 reflection for the superlattices with $PbTiO_3$ layer thicknesses $n = 22$, 20, 15 and 12. **b** Line cuts along the dashed lines in (a), showing in-plane ordering across the first-order superlattice peaks. **c** In-plane periodicity and average lattice constant *c* as a function of *n*. **d, e** Selected diffraction intensity region in the *H0L*-slice RSM around LSAT 002 (d) and corresponding X-ray nanobeam diffraction map (**e**) for the $n = 12$ superlattice. **f, g** Selected diffraction intensity region in the *H0L*-slice RSM around LSAT 002 (f) and corresponding X-ray nanobeam diffraction map (g) for the $n = 15$ superlattice. Scale bar = 2 μm. **h** Cross-sectional HAADF-STEM image of the $n = 22$ superlattice, which clearly displays the interfaces between the component layers. **i, j** High-resolution HAADF image (background) and reconstructed polarization vectors (arrows) of the $n = 22$ (**i**) and $n = 12$ (**j**) superlattices. The orange dots mark the core position of the vortex-like topological structures, showing the ordering across the layers along the out-of-plane direction. The black/white color contrast in the HAADF images (**h**–**j**) denotes low/high scattering intensity of atomic columns.

typical results of a dipole wave structure for $n = 12$ and a flux closure structure for $n = 22$, both assigned according to the original structure models[8,9]. We consider that the $n = 15$ and 20 superlattices have similar structures as $n = 12$ and 22, respectively, and therefore divide them into two groups: dipole waves for $n = 12$ and 15, and flux closures for $n = 20$ and 22, as the *n* is closer in each group than between the two groups. Furthermore, the individual dipole wave or flux closure structures appear to be well aligned vertically across multiple $PbTiO_3$ layers (see their cores marked in Fig. 1i, j), consistent with the X-ray RSM results. Previous studies have reported vortex-antivortex pairs in superlattices with similar $PbTiO_3$ and $SrTiO_3$ layer thicknesses[12]. In our superlattices, the difference in misfit strain and other factors may have led to the observed topological structures (see Supplementary Note 4).

Ferroelectric switching and low-frequency electric measurements

The in-plane ferroelectric switching properties of the superlattices were measured on coplanar capacitors with interdigitated electrodes (IDEs), as shown in the inset of Fig. 2a. Owing to the complex electrical attributes of IDEs, the polarization and capacitance are shown as charge or capacitance per unit length of electrode. The measured polarization–electric field (*P*–*E*) loops at 10 kHz display nonzero in-plane net polarization P_x and ferroelectric-like hysteresis at the initial state in all the superlattices (Fig. 2a). This in-plane polarization matches the polar structures shown in Fig. 1i, j, where larger areas with in-plane polarization along +*x* direction than the negligible ones along -*x* direction prevent the polarization from canceling out, enabling the

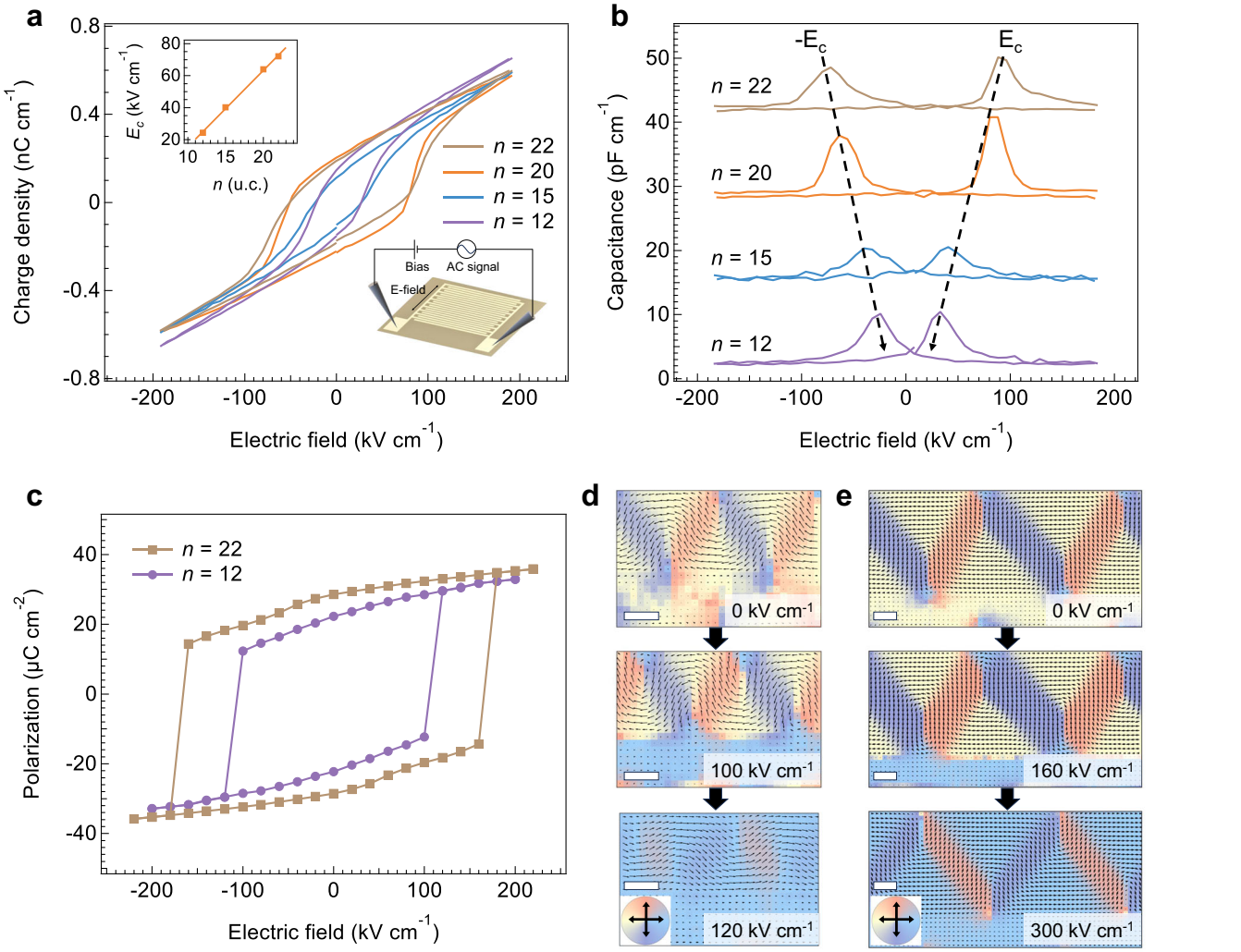

Fig. 2 | Ferroelectric switching behaviors of the superlattices. a Measured *P*–*E* loop of the superlattices, with polarization displayed as charge density per unit length of interdigitated electrodes. Insets: schematic of the *P*–*E* loop measurement and the derived switching field E_c as a function of $PbTiO_3$ layer thickness *n*. **b** Differential capacitance curves as a function of electric field obtained from (a), showing dielectric peaks at the switching fields. Offsets are applied for clarity. **c** Simulated *P*–*E* loops for the *n* = 12 and 22 superlattices from MD simulations. **d**, **e** Simulated polarization evolution under in-plane electric field for the *n* = 12 (**d**) and *n* = 22 (**e**) superlattices. The arrows denote local polarization vectors, and the color wheels represent the direction. Scale bar = 2 nm.

ferroelectric-like switching process. Capacitance–voltage (*C*–*V*) loop can be derived from the *P*–*E* loop by extracting the polarization change rate with respect to the external voltage variation[43], as shown in Fig. 2b. The peaks of these butterfly-shaped loops are located at the coercive field E_c, with the highest polarization change rate. The coercive field E_c increases with increasing $PbTiO_3$ layer thickness *n* in a nearly linear manner (Fig. 2a inset), similar to the trend of in-plane periodicity, suggesting a correlation between the in-plane switching dynamics and periodicities of the topological polar structures.

The observed correlation is further corroborated by molecular dynamics (MD) simulations. The simulation results (Fig. 2d, e) indicate a two concurrent in-plane switching processes: the major switching process in the $PbTiO_3$ layers when the net polarization changes direction, in addition to a minor polarization switching in the $SrTiO_3$ layers (contributing ~12% to total polarization at the highest field) which has little influence on the net polarization and thus is invisible in the *P*–*E* loop. With an electric field applied along the +*x* direction, the areas with the opposite in-plane polarization (yellow areas in Fig. 2d, e) shrink, and those with out-of-plane polarization directions (red and blue areas) expand, revealing the polarization rotation from the in-plane to out-of-plane directions[44]. With further increase in the electric field, the polarization in-plane flips towards the electric field direction, completing the switching process in the $PbTiO_3$ layers. Upon removal of the electric field, the topological structure recovers in the new in-plane polarization direction (Supplementary Fig. 6), corresponding to the remanent polarization in the *P*–*E* loop. However, such switching processes result in different final states for different topological structures. In the dipole wave structure with smaller *n*, the superlattice turns into a single *a*-domain with minor out-of-plane polarization after switching, thereby losing almost all topological features. In the flux closure structure with larger *n*, the topological features are maintained after switching, suggesting better stability and topological protection of the flux closure. This results in a larger coercive field for the flux closure (Fig. 2c), as a higher energy barrier has to be overcome to perturb a more stable topological phase, consistent with the experimental observations. The calculated coercive fields are a few times larger than the experimental values and thus represent the intrinsic values; in the real superlattices, defects may have lowered the energy barrier for polarization switching.

Structural evolution during ferroelectric switching

To probe the structural evolution of the topological polar phases during switching, second harmonic generation (SHG) mapping under normal incidence was conducted before and after the switching

https://doi.org/10.1038/s41467-026-69440-x

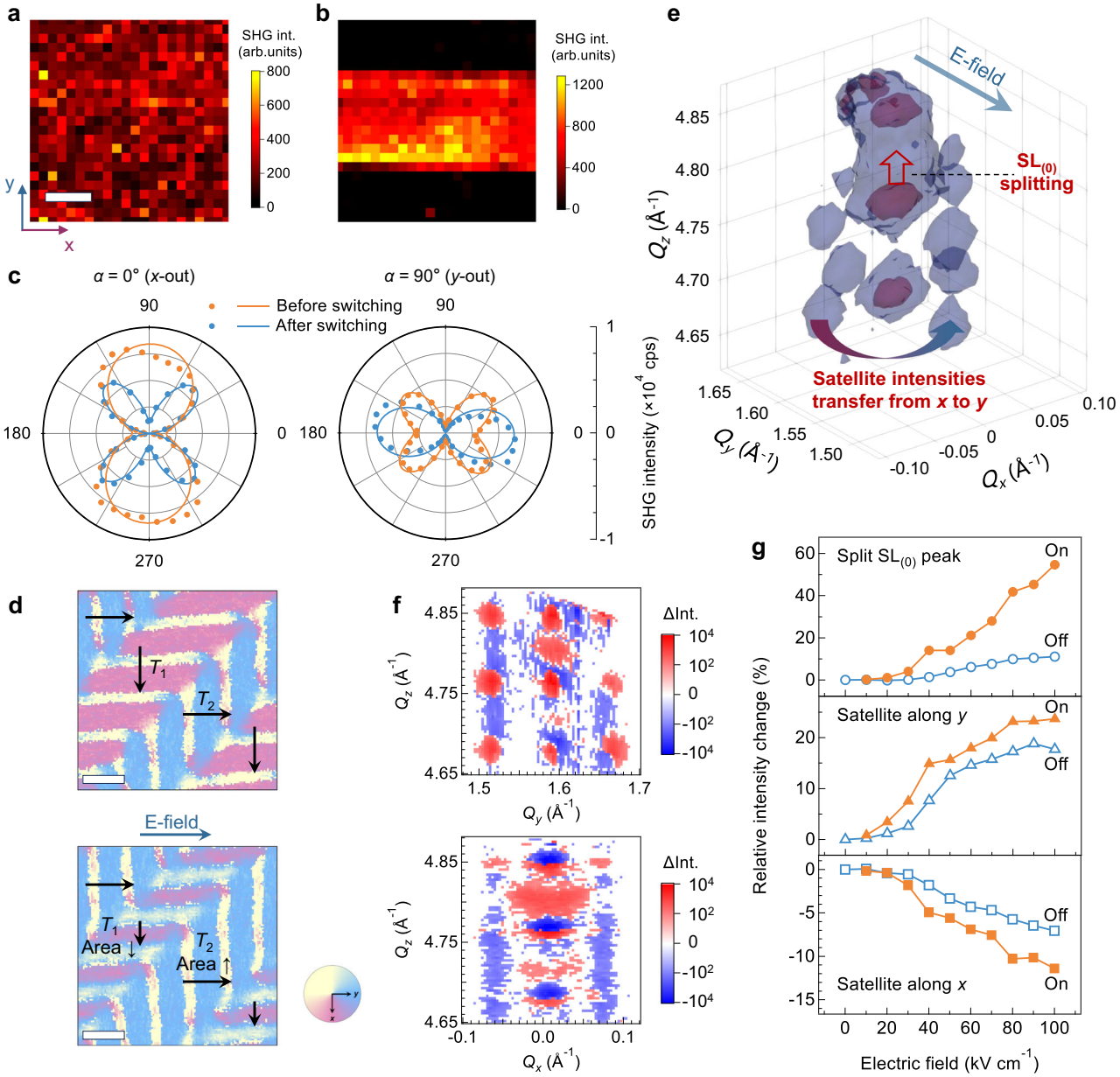

Fig. 3 | Microscopic evidence for field-induced structural evolution. a–c SHG measurements of the $n = 15$ superlattice, including SHG images outside the IDE areas/before switching (**a**) and inside the IDE areas/after switching (**b**) along with the corresponding SHG polarimetry plots (**c**). Scale bar = 5 μm. **d** MD simulations of the polarization switching process in the *xy*-plane within $PbTiO_3$ layers for the $n = 12$ superlattices. Colors and arrows correspond to the direction of net polarization for the area. The applied electric field is along the *y*-axis. Scale bar = 10 nm. **e** 3D RSM for the $n = 12$ superlattice, with arrows illustrating the measured diffraction intensity changes. Blue and red colors show contour surfaces of the diffraction intensity of 1100 and 7000 arbitrary units, respectively. **f** Difference maps of the *yz*- and *xz*-RSM slices between the "off" states at 100 V and the initial state at 0 V. **g** Intensity evolution of the satellite peaks and split zeroth-order superlattice peak at Q_z of approximately 4.80 $Å^{-1}$ as a function of the electric field for both the "on" and "off" states.

process[45]. The mapping results for both dipole wave and flux closure superlattices (Fig. 3a and Supplementary Fig. 2a) show uniform SHG intensities in the pristine area. Post-switching SHG mapping within the IDE fingers (Fig. 3b and Supplementary Fig. 2b) reveals a nearly uniform contrast with ~3 times stronger SHG intensities, suggesting an enhancement of the in-plane polarization component. SHG polarimetry analysis (Fig. 3c and Supplementary Fig. 2c) further reveals changes in the lattice anisotropy of the topological polar phases. Both the $\alpha = 0°$ and $\alpha = 90°$ polar plots show a mixture of twofold intensity lobes and 45°-oriented fourfold lobes outside the IDEs. The twofold component at $\alpha = 0°$ and the fourfold component at $\alpha = 90°$ disappears inside the IDEs after switching. This evidences a nonvolatile symmetry change during polarization switching, which persists after field removal.

The second-order nonlinear susceptibility tensors ($\chi^{(2)}$) were obtained from fittings to the SHG polarimetry patterns (see details in Supplementary Note 1). According to the symmetry of the topological polar structures and the coordinate transformation methods previously described[46], the twofold-fourfold mixture in the SHG originates from coexisting a_1/a_2-like domains. We use T_1/T_2 to denote the topological structures with different net in-plane polarization directions, thus to distinguish from the conventional a_1/a_2 domain nomenclature. As shown by the simulation results in Fig. 3d, these T_1/T_2 domains form a hatched pattern, similar to previous observations in polar

vortices[18,47]. The changes in their populations during switching are obtained from the measured SHG patterns (see Supplementary Table 2). For the $n = 15$ superlattice, the proportion of T_1 domains (dipole wave) decreases from 62.6% to 29.3% after switching, whereas the T_1 domains (flux closure) for $n = 22$ decrease from 51.6% to 29.5%, both shifting away from 50%. This indicates a breaking of the *x*-/*y*-, two equivalent in-plane directions due to the applied electric field, corresponding to the 90° polarization switching from T_1 to T_2 domains, as shown in Fig. 3d.

Synchrotron-based in situ 3D RSM measurements were performed to obtain the microscopic information during switching in the dipole wave superlattice with $n = 12$, as presented in Fig. 3e–g and Supplementary Fig. 3. When an electric field is applied ("on" state, Supplementary Fig. 3b) along the *y*-direction, the satellite diffraction intensity transfers from the *x*- to *y*-direction, and meanwhile, the zeroth-order superlattice ($SL_{(0)}$) peak splits, shifting toward a higher Q_z, as illustrated in Fig. 3e. The observed intensity transfer corresponds to the previously described polarization switching from T_1 to T_2 domains. The zeroth-order peak splitting results from dipole waves switching to conventional ferroelectric *a*-domains, which transition reduces the out-of-plane polarization component, thus shrinking the lattice constant *c* from 3.960 Å to 3.926 Å (-0.86% change). Such an induced transition implies that the $n = 12$ superlattice is close to the phase boundary of dipole waves and *a*-domains, consistent with the XRD results for the pristine state (Fig. 1d, e).

Upon removal of the electric field ("off" state, Fig. 3f), the induced intensity transfer and peak splitting are partially reversed, but the intensities of both the split zeroth-order peak and satellite peaks along the *y* direction remain higher than those in the pristine state. These remanent changes indicate a larger proportion of T_2-domains along with the existence of *a*-domains compared with the pristine state. Figure 3g presents the field evolution of diffraction intensities for both "on" and "off" states. Overall, major intensity changes occur at approximately 40–50 kV cm^{-1}, which agrees with the coercive field observed in the *P*–*E* loops (Fig. 2a). For the satellites along the *y*-axis, a maximum intensity increase of ~24%/18% for the "on/off" state, suggesting a ~ 20% increase in the proportion of T_2 domains.

Millimeter-wave dielectric measurements

Millimeter-wave dielectric constants within the 2–110 GHz frequency range were measured via coplanar waveguides (CPWs) fabricated on the superlattices, with d.c. bias voltages applied between the ground and signal lines to measure the dielectric tunability, as illustrated in Fig. 4a (see details in Methods). The complex dielectric constants ε_r for different superlattices at zero d.c. voltage are shown in Fig. 4b, c, which serve as a baseline for the tunability calculation. The real part of ε_r (ε_r') decreases monotonically while the imaginary part (ε_r'') increases as the measuring frequency increases. These trends agree with the Cole-Cole relaxation model which describes the complex permittivity $\varepsilon^*(\omega)$ as[48,49]:

$$\varepsilon^*(\omega) = \varepsilon_\infty + \frac{\varepsilon_s - \varepsilon_\infty}{1 + (i\omega\tau)^\beta} \quad (1)$$

where ε_s is the static dielectric permittivity, ε_∞ the "infinite frequency" permittivity, τ the relaxation time constant, and β is a parameter describing the distribution width of relaxation times. The fitted τ for all the superlattices is on the scale of ~1 ps (Fig. 4d), suggesting rapid polarization responses. The dipole waves ($n = 12$ and 15) exhibit twice larger τ, in agreement with their stronger frequency dispersion of ε_r' than the flux closures ($n = 20$ and 22). The superlattices exhibit relatively large loss tangents ($\varepsilon_r'/\varepsilon_r''$) above 40 GHz, ranging from approximately 0.2 to 0.5. This high loss is likely dominated by defect-related contributions[35], representing a drawback for applications. However, it could be mitigated through optimized thin-film growth processes, which hold promise for reducing defect densities.

The *C*–*V* curves were measured by sweeping a.c. frequencies as a function of d.c. bias voltages. The results at 20 GHz are illustrated in Fig. 4e for different superlattices (see Supplementary Fig. 4 for the results at other frequencies), and the dielectric tunability, calculated by $|\Delta\varepsilon_r'|/\varepsilon_r'(0\ \mathrm{V})$, is presented in Fig. 4f. For the flux closures ($n = 20$ and 22), the measured tunability is only approximately 2% in the range of 30 kV cm^{-1}, consistent with their higher coercive fields hindering polarization switching. For the dipole waves, the in-plane polarization switching process introduces a decrease in the dielectric constant, resulting in over 5% tunability observed in all $n = 12$–17 superlattices. Under 30 kV cm^{-1}, the $n = 17$ superlattice exhibits the largest dielectric tunability of ~20% at 20 GHz, which remains relatively stable in the entire measured frequency range: >15% at 70 GHz and >8% at 110 GHz. The lower overall dielectric tunability of the $n = 12$ superlattice may be attributed to the coexistence of dipole waves and tilted *a*-domains (see Fig. 1d, e). Similar *a*-domains in single-layer $PbTiO_3$ films grown on $SrTiO_3$ substrates showed minimal tunability (~2%) under 700 kV cm^{-1}, a negligible response compared with the low-field conditions in our measurements[19]. Considering the tilted *a*-domain and dipole wave structures behave as capacitors in series, the overall dielectric permittivity should be a weighted average of the two structure types, whereby an almost field-independent permittivity of the *a*-domains considerably reduces the overall dielectric tunability. The high overall dielectric tunability in the $n = 17$ superlattice correlates with its large zero-field permittivity, suggesting that the dynamical polarization response is enhanced near the topological phase boundaries between dipole wave and flux closure structures.

MD simulations were performed to further correlate the dielectric tunability with the structural changes during polarization switching. The dielectric constant ε_r was evaluated from the simulated time-domain polarization evolution upon the excitation of a Gaussian electric field pulse (see details in Supplementary Note 2). Figure 4g presents the simulated dielectric constants under varying excitation fields, which manifest larger permittivity and tunability values in the dipole wave than the flux closure structure, well corroborating the measurement results. The structural origin of such differences is illustrated in Fig. 4h for the zero-bias case. In the dipole wave structure, the wavy area with large out-of-plane polarization components (see the blue-shadowed region in Fig. 1j) exhibits prominent local in-plane polarization response, indicating an instantaneous polarization rotation following the millimeter-wave electric field. This leads to large average polarization changes (denoted by ΔP_y) in the whole superlattice, and thus higher dielectric permittivity. By contrast, the area with discernible local ΔP_y in the flux closure structure concentrates along the 90°-domain walls, corresponding to the in-plane domain switching process similar to the low-frequency transitions (Fig. 2e). However, the polarization response is marginal in the domain interior, thus amounting to considerably smaller average ΔP_y and lower dielectric permittivity.

Supplementary Fig. 9 (see also Supplementary Movie 1) illustrates the simulated millimeter-wave dielectric responses under applied d.c. bias fields. Although the dipole wave topology itself is transformed due to the low-frequency switching process (Fig. 2d), the original wavy area in the structure still displays high local ΔP_y under the d.c. bias, similar to its zero-bias response behavior. This indicates that its remnant minor out-of-plane polarization can still rotate to the in-plane direction upon the millimeter-wave excitation. The ΔP_y in the dipole wave under the d.c. bias is smaller than that without bias, yet still larger than that in the flux closure. The latter structure retains its topological features after the low-frequency switching, and similarly exhibits minor ΔP_y concentrated along the domain walls.

Figure 4i further compares the frequency spectra of the simulated and measured dielectric tunability in the dipole wave, both of which show broad peaks around 20–30 GHz and 40–50 GHz. This possibly hints at the existence of collective modes in the dipole wave structure,

https://doi.org/10.1038/s41467-026-69440-x

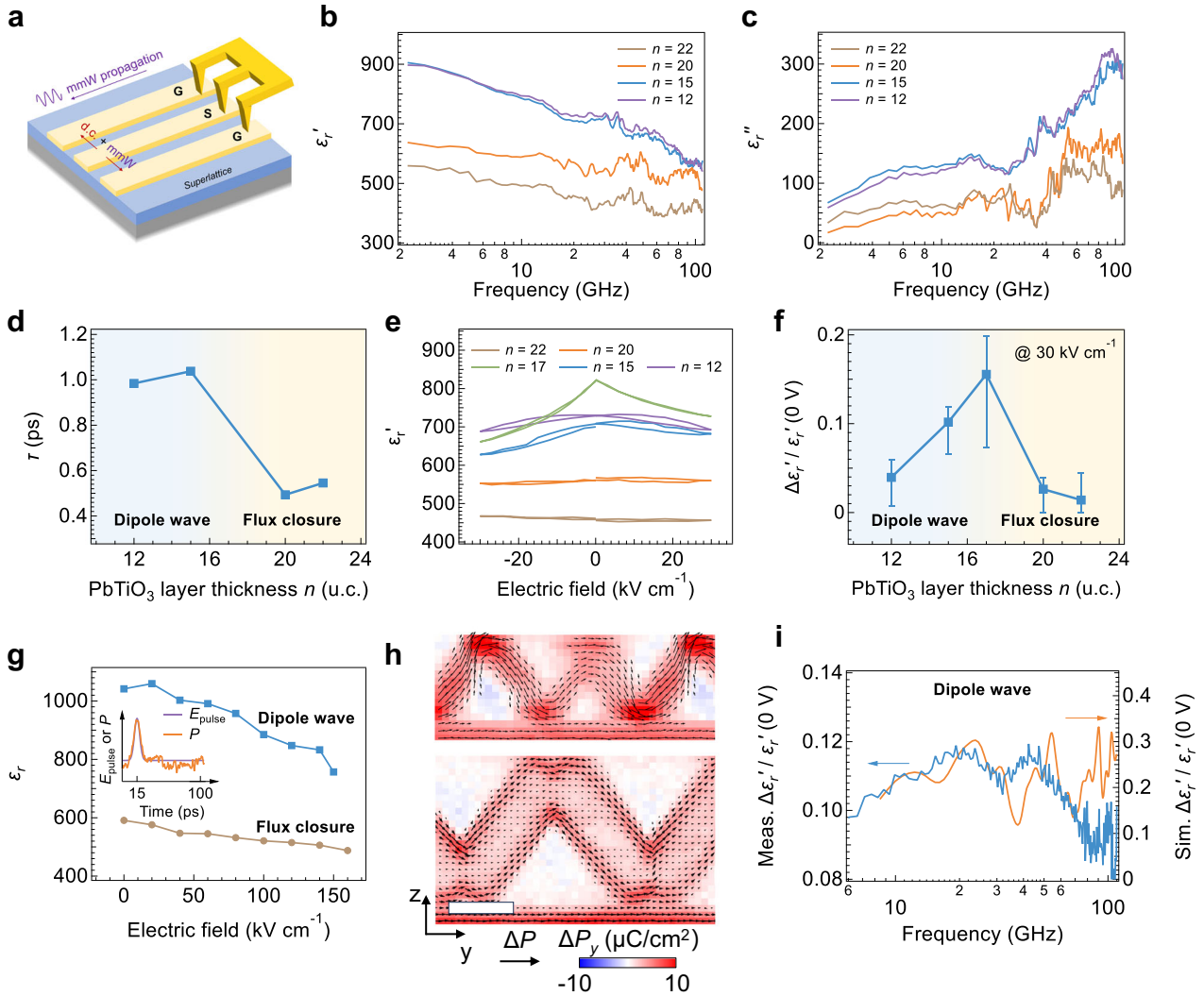

Fig. 4 | Dielectric tunability at millimeter-wave frequencies. a Schematic of the CPW device fabricated on the superlattices, accessed via a pair of ground-signal-ground (GSG) probes. **b, c** Measured dielectric frequency spectra of the superlattices, including the real (**b**) and imaginary (**c**) parts of the in-plane dielectric constant under zero field. **d** Fitted relaxation time constant τ as a function of the $PbTiO_3$ layer thickness n. **e** Dependence of the real part dielectric constant on the d.c. electric field, all measured at 20 GHz. **f** Dielectric tunability at 70 GHz as a function of n. The error bars represent the variations across 2–110 GHz. **g** Dependence of the real part dielectric constant at 20 GHz on d.c. electric field, obtained via MD simulations. Inset: schematic of evaluating the dielectric response by applying a pulsed electric field in the MD model. **h** Simulated polarization changes (ΔP) in the dipole wave (top) and flux closure (bottom), at the maximum excitation amplitude of a 20 GHz sinusoidal electric field ($t = 12.5$ ps), compared to the equilibrium state ($t = 0$) without d.c. bias. Scale bar = 4 nm. **i** Simulated dielectric frequency spectrum of the dipole wave system compared with the experimental results for the $n = 15$ superlattice. Both spectra are normalized against the zero-field values.

with frequencies in the same order with the modes observed in polar vortices (around 80 GHz)[22]. Another possible contribution to the dielectric tunability is the resonant switching from T_1 to T_2 domains (Fig. 3d). As shown in Supplementary Fig. 10, upon application of a combination of d.c. and 20 GHz a.c. electric fields, the T_1/T_2 proportion further decreases, lower than that under a d.c. field with the same magnitude. Similar resonant switching processes have been reported in a previous study on polar vortices[50]. This process further reduces the overall dielectric permittivity under electric fields, leading to higher dielectric tunability. Taken together, the MD simulations clearly delineate the structural dynamics underlying the large dielectric tunability of the dipole wave.

Discussion

Figure 5 presents the dielectric tunability as a function of operating frequency of the dipole waves in the $n = 17$ superlattice, together with that of multiple materials reported in previous studies. Due to the relatively low applied electric fields in our measurements (up to 30 kV cm^{-1}), the maximum tunability of the dipole waves is smaller than that reported for some of these materials. Therefore, the tunability slope with respect to the electric field, as shown in Fig. 5, represents a more intrinsic metric for performance comparison. Notably, the dipole waves exhibit a higher tunability slope than most of the reported materials, particularly at frequencies exceeding 20 GHz. This behavior indicates strong potential for achieving substantially higher tunability in dipole waves under larger applied electric fields.

The understanding of microscopic polarization dynamics underpins the prediction of the dielectric response of topological polar phases. Fitting the dielectric tunability for the $n = 15$ superlattice with a phenomenological model described in the literatures[51,52] extrapolates the tunability under an elevated electric field of 400 kV cm^{-1} to be 60–65% at 110 GHz. This performance is significantly advantageous over other ferroelectric materials at high frequencies (70–110 GHz), for example, $(Ba,Sr)TiO_3$ (46% under 400 kV cm^{-1})[35] and $HfZrO_2$ (10%

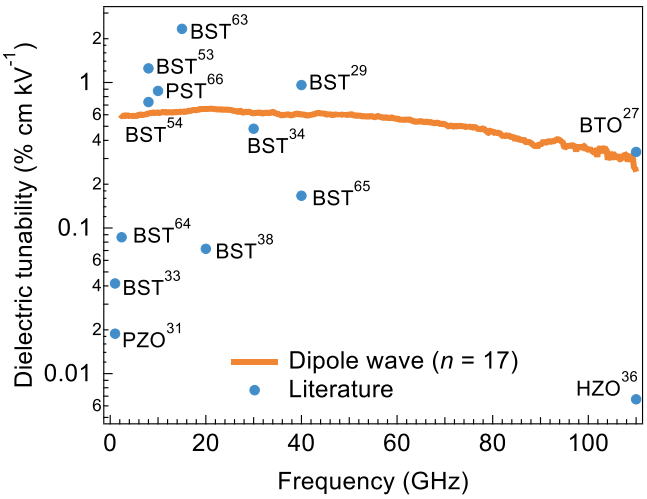

Fig. 5 | Comparison of the tunability slope as a function of operating frequency of dipole waves and representative materials reported in previous studies. The materials and associated studies included are as follows: $BaTiO_3$ (BTO)[27], (Ba,Sr)TiO_3 (BST)[29,33,34,38,53,54,63–65], $PbZrO_3$ (PZO)[31], $HfZrO_2$ (HZO)[36], and (Pb,Sr)TiO_3 (PST)[66].

under 3 MV cm^{-1} in vertical film capacitors)[36], although (Ba,Sr)TiO_3 systems display higher tunability at lower frequencies (below 40 GHz)[34,38,53,54]. Additionally, the relatively stable tunability up to 110 GHz measured in the $n = 15$ and 17 superlattices suggests higher response frequencies towards the terahertz range.

In summary, we have observed the millimeter-wave dielectric tunability in $(PbTiO_3)_n/(SrTiO_3)_8$ superlattices driven by the polarization dynamics of the underlying topological polar structures. The $n = 15$ and 17 superlattices with dipole waves exhibit a large dielectric tunability of over 8% in the measured 2–110 GHz frequency range under an in-plane electric field of 30 kV cm^{-1}, with further potential for increased tunability under elevated electric fields. This tunability performance is significant compared with those of conventional ferroelectric materials, especially at high frequencies over ~70 GHz. Both the dipole waves and flux closures exhibit in-plane polarization switching behaviors, during which process the topological structures with a net in-plane polarization direction orthogonal to the applied electric field rotate towards the latter direction, and the observed switching characteristics link the origins of their dielectric tunabilities. We have established the mechanisms between the microscopic polarization dynamics and macroscopic permittivity through combined experimental and theoretical methods. Our study thus demonstrates an effective and generalizable framework for predicting high-frequency dielectric properties of topological polar systems, which can incorporate more degrees of freedom for material optimization such as substrate strain engineering. Besides, the integratable thin-film superlattices provide a viable platform for constructing on-chip dielectric tuning devices in the millimeter-wave frequency range. Collectively, this study reveals the inherent potential of topological polar structures for enabling high-speed integrated devices, such as phase shifters and reconfigurable antennas, for next-generation millimeter-wave communication and sensing technologies.

Methods

Superlattice growth

$(PbTiO_3)_n/(SrTiO_3)_8$ superlattices were grown on (001)-cut $(LaAlO_3)_{0.3}$-$(SrAl_{0.5}Ta_{0.5}O_3)_{0.7}$ (LSAT) single crystal substrates via reflection high-energy electron diffraction-assisted pulsed laser deposition (PLD), with a 5-nm buffer layer of $GdScO_3$ to relax the in-plane substrate strain. A 248 nm KrF excimer laser (COMPex205, Coherent) was used to ablet the corresponding ceramic targets with a laser fluence and repetition rate of 1.1 J cm^{-2}/3 Hz for $GdScO_3$, 1.2 J cm^{-2}/5 Hz for $PbTiO_3$, and 1.2 J cm^{-2}/3 Hz for $SrTiO_3$. The $GdScO_3$ and superlattice layers were grown at temperatures of 770 °C and 650 °C, at oxygen pressures of 5 Pa and 12 Pa, respectively. The superlattice films were then annealed for 10 min at 650 °C, followed by cooling to room temperature at a cooling rate of 60 °C min^{-1} under an oxygen pressure of 20 kPa.

X-ray diffraction

Laboratory-based $2\theta/\omega$-coupled scans and reciprocal space mapping (RSM) measurements were performed with a high-resolution X-ray diffractometer (SmartLab 9 kW, Rigaku) using Cu $K\alpha_1$ radiation ($\lambda = 1.5406$ Å). A 2D area detector (HyPix-3000) was used to collect the diffraction signals.

In situ electric field dependent three-dimensional reciprocal space mapping (3D RSM) was performed at the BL13XU beamline of Super Photon ring-8 GeV (SPring-8) synchrotron. A monochromated X-ray beam with a photon energy of 12.4 keV ($\lambda = 1$ Å) was used. The beam was focused to a size of 12 × 21 μm^2 on the sample surface between the interdigitated electrodes (described below). The sample was mounted on a four-circle diffractometer, connected to an external voltage generator with a tungsten probe station to apply an in-plane electric field. A 2D photo-counting detector (PILATUS3 300 K) was used to record the diffraction signals. The 3D RSM results were reconstructed from raw measured data using custom Python codes.

Synchrotron X-ray nanobeam diffraction experiments were performed at the hard X-ray nanoprobe at station 26-ID-C of the Advanced Photon Source at Argonne National Laboratory. A monochromated X-ray beam with a photon energy of 10 keV and a focal spot size of 50 nm was used. The beam was focused to a footprint of ~50 × 160 nm^2 on the sample surface. A 2D area detector positioned 1000 mm from the sample was used to record the diffraction signals.

Scanning transmission electron microscopy

Cross-sectional thin specimens of the superlattices were prepared using a focused ion beam on a dual-beam microscope (Nova Nanolab 200, Thermo Fisher Scientific) or ion milling (PIPS Model 695, Gatan) after mechanical polishing. STEM observations were performed on a double-aberration-corrected transmission electron microscope (Spectra 300, Thermo Fisher Scientific), operated at an accelerating voltage of 300 kV. High-angle annular dark-field (HAADF) STEM images were collected with a probe convergence angle of 25.0 mrad and an inner detector angle of 49 mrad. Positions for all atomic columns in the HAADF images were obtained by 2D Gaussian fits using Matlab codes[55]. Displacement vectors of B-site columns were calculated based on local offsets of their sublattice relative to the A-site sublattice. The direction of spontaneous polarization in each unit cell is opposite to the direction of B-site displacement.

Second-harmonic generation

SHG measurements were performed on a home-developed microscope system[45]. A Ti: sapphire femtosecond laser (MaiTai, Spectra-Physics) with 35 fs pulse width, 800 nm wavelength, and an average power of 25 mW was used as the 1ω excitation source. Normal incidence geometry was applied in the measurements, where the 1ω laser beam was focused on the top surface of the film using an objective lens (numerical aperture = 0.55), and the backscattered 2ω signals were also collected by the lens. A zero-order half-waveplate was used to control the 1ω excitation light polarization, and a Glan-Taylor prism polarizer was used to analyze the 2ω signal polarization. A photomultiplier tube detector was used to record the 2ω light signal after band-pass filtering to exclude 1ω light signals.

Low-frequency electric measurements

Interdigitated electrodes (IDEs) of 200 nm Au/Ti were fabricated on the surface of the superlattice films via standard photolithography lift-

off and sputtering techniques, with 20 μm wide electrode conductors and 10 μm gaps between these parallel conductors. The effective length of the IDEs is 1.000 mm, with 9 and 19 effective capacitor gaps in 5-pair and 10-pair IDEs, respectively. The voltage-dependent capacitance was measured via an impedance analyzer (E4990A, Keysight) with a built-in voltage source. The ferroelectric switching properties were measured with a ferroelectric tester (10-kV HVI-SC, Radiant Technology).

Millimeter-wave dielectric measurements

Coplanar waveguides (CPWs) with a cross-section comprising an 11 μm center conductor, a 15 μm gap and a 200 μm ground plane were fabricated on the superlattice films via the same processes as the IDEs. Five different effective lengths ranging from 0.260 mm to 1.740 mm were designed, together with a short-circuit reflection calibration device matching the shortest length. CPWs on all the superlattices and a bare LSAT substrate were fabricated in the same batch to ensure consistent device electrode thicknesses and shapes. The complex S-parameters of the CPW devices ranging from 2 GHz to 110 GHz were measured via a millimeter-wave vector network analyzer (N5290A, Keysight) coupled with a probe stage (EPS200MMW, FormFactor) and a pair of ground-signal-ground (GSG) probes. D.c. voltages between the ground and signal lines were applied via a source meter (Keithley 2470).

A multiline TRL approach employing a Python package by Ziad Hatab[56] was then applied for initial calibration to obtain the propagation constant $\gamma_0 = \sqrt{R + i\omega L}\sqrt{G + i\omega C}$, of the transmission line from the S-parameters, where R, L, C, and G represent distributed resistance, inductance, capacitance, and conductance per unit length, respectively, and ω denotes the angular frequency. R, L, C, and G of the transmission lines on LSAT substrates and films were simulated with Q3D module in Ansys Electronics Desktop Student with a 2-D cross-sectional model. The dielectric constant of LSAT and the conductivity of the metal layers can then be obtained by comparing γ_0 calculated from the simulations and from the experimental S-parameters. The R and L on all the superlattice samples should be identical to those on the LSAT substrate, as the geometric structure and conductivity of the metal layers are identical. The C and G for the superlattices were then calculated from γ_0 and above, simulated R and L. A functional relationship between the C, G and complex dielectric constant of the superlattice layer was established by mapping the dielectric constant and loss of the film in the 2-D model, which was later used to extract dielectric constants under different voltages and frequencies from the above calculated C and G.

Molecular dynamics simulations

Molecular dynamics (MD) simulations were conducted using a machine learning-based force field capable of modeling various topological structures[57,58]. To simulate the dipole wave and flux closure state, the number of layers in $SrTiO_3$ was fixed at 8, while the layers in $PbTiO_3$ were varied from 12 to 22. All MD simulations were carried out in the isobaric-isothermal (*NPT*) ensemble using LAMMPS[59]. The temperature and pressure was maintained at 300 K and 1.0 bar using the Nosé-Hoover thermostat and Parrinello-Rahman barostat, respectively. A timestep of 2 fs was utilized, with each simulation consisting of a 50 ps equilibrium run followed by a 50 ps production run. Initial and final configurations are given in Supplementary Data 1.

Once equilibrium was achieved under zero electric field conditions, an electric field was gradually increased to 200 kV cm^{-1} across the superlattice to obtain the P–E loop. The interaction between the electric field and each ion was determined by multiplying the electric field strength by the Born effective charge (BEC) tensor of the corresponding ion. Density functional theory (DFT) calculations were used to determine BEC values, as shown in Table 1. All DFT calculations were performed with a plane-wave basis utilizing the Vienna Ab initio Simulation Package (VASP)[60,61]. The exchange-correlation functional used was the Perdew-Burke-Ernzerhof functional modified for solids (PBEsol)[62], with an energy cutoff of 800 eV and a k-point spacing of 0.3 Å^{-1}.

Table 1 | BEC tensors used in MD simulations for $PbTiO_3$ and $SrTiO_3$. Z_{11}^*, Z_{22}^*, and Z_{33}^* denote the diagonal components of the BEC tensor

System	Z_{Pb}^* or Z_{Sr}^* (e)			Z_{Ti}^* (e)			Z_O^* (e)		
	Z_{11}^*	Z_{22}^*	Z_{33}^*	Z_{11}^*	Z_{22}^*	Z_{33}^*	Z_{11}^*	Z_{22}^*	Z_{33}^*
$PbTiO_3$	3.74	3.74	3.45	6.17	6.17	5.21	−3.30	−3.30	−2.89
$SrTiO_3$	2.56	2.56	2.56	7.40	7.40	7.40	−3.32	−3.32	−3.32

Data availability

Source Data are provided with this paper. Other data supporting this study, including the training database and input files for MD and DFT calculations, are available on Zenodo (https://doi.org/10.5281/zenodo.18316581). All other data that support the findings of this study are available from the corresponding authors upon request. Source data are provided with this paper.

Code availability

Molecular dynamics simulations were performed using the open-source LAMMPS package (https://github.com/lammps/lammps). The Vienna Ab initio Simulation Package (VASP) used for DFT calculations can be obtained after completing a license agreement on its official website.

References

1. Zhou, L. et al. Local manipulation and topological phase transitions of polar skyrmions. *Matter* **5**, 1031–1041 (2022).
2. Yadav, A. K. et al. Observation of polar vortices in oxide superlattices. *Nature* **530**, 198–201 (2016).
3. Li, Q. et al. Quantification of flexoelectricity in $PbTiO_3/SrTiO_3$ superlattice polar vortices using machine learning and phase-field modeling. *Nat. Commun.* **8**, 1468 (2017).
4. Das, S. et al. Observation of room-temperature polar skyrmions. *Nature* **568**, 368–372 (2019).
5. Wang, Y. J. et al. Polar meron lattice in strained oxide ferroelectrics. *Nat. Mater.* **19**, 881–886 (2020).
6. Rusu, D. et al. Ferroelectric incommensurate spin crystals. *Nature* **602**, 240–244 (2022).
7. Junquera, J. et al. Topological phases in polar oxide nanostructures. *Rev. Mod. Phys.* **95**, 025001 (2023).
8. Gong, F.-H. et al. Atomic mapping of periodic dipole waves in ferroelectric oxide. *Sci. Adv.* **7**, eabg5503 (2021).
9. Tang, Y. L. et al. Observation of a periodic array of flux-closure quadrants in strained ferroelectric $PbTiO_3$ films. *Science* **348**, 547–551 (2015).
10. Wang, Z. & Chen, L.-Q. Tuning Topology Phases by Controlling Effective Screening and Depolarization in Oxide Superlattices. *Nano Lett* **24**, 5761–5766 (2024).
11. Tong, P. et al. Thermal triggering for multi-state switching of polar topologies. *Nat. Phys.* **21**, 464–470 (2025).
12. Abid, A. Y. et al. Creating polar antivortex in $PbTiO_3/SrTiO_3$ superlattice. *Nat. Commun.* **12**, 2054 (2021).
13. Zhu, R. et al. Atomic-scale tracking topological phase transition dynamics of polar vortex-antivortex pairs. *Adv. Mater.* **36**, 2312072 (2024).
14. Hong, Z. et al. Stability of polar vortex lattice in ferroelectric superlattices. *Nano Lett* **17**, 2246–2252 (2017).
15. Damodaran, A. R. et al. Phase coexistence and electric-field control of toroidal order in oxide superlattices. *Nat. Mater.* **16**, 1003–1009 (2017).

16. Wang, S. et al. Giant electric field-induced second harmonic generation in polar skyrmions. *Nat. Commun.* **15**, 1374 (2024).
17. Behera, P. et al. Electric field control of chirality. *Sci. Adv.* **8**, eabj8030 (2022).
18. Kavle, P. et al. Highly responsive polar vortices in all-ferroelectric heterostructures. *Adv. Mater.* **36**, 2410146 (2024).
19. Das, S. et al. Local negative permittivity and topological phase transition in polar skyrmions. *Nat. Mater.* **20**, 194–201 (2021).
20. Huang, S., Ma, C. & Jin, K. Advanced ferroelectric oxide films and heterostructures for unconventional applications. *Adv. Phys. X* **10**, 2438686 (2025).
21. Luo, S. S. et al. Modulation of flux-closure polar state for enhanced storage unit and thermal conductivity via dual-probe excitation. *J. Appl. Phys.* **137**, 014102 (2025).
22. Li, Q. et al. Subterahertz collective dynamics of polar vortices. *Nature* **592**, 376–380 (2021).
23. Stoica, V. A. et al. Optical creation of a supercrystal with three-dimensional nanoscale periodicity. *Nat. Mater.* **18**, 377–383 (2019).
24. Yang, T., Dai, C. & Chen, L.-Q. Thermodynamics of light-induced nanoscale polar structures in ferroelectric superlattices. *Nano Lett* **23**, 2551–2556 (2023).
25. Li, W. et al. Terahertz excitation of collective dynamics of polar skyrmions over a broad temperature range. *Nat. Phys.* **21**, 1965–1972 (2025).
26. Maiwald, T. et al. A review of integrated systems and components for 6G wireless communication in the *D* -Band. *Proc. IEEE* **111**, 220–256 (2023).
27. Cochard, C., Spielmann, T. & Granzow, T. Dielectric tunability of ferroelectric barium titanate at millimeter-wave frequencies. *Phys. Rev. B* **100**, 184104 (2019).
28. Pesquera, D. et al. Beyond substrates: strain engineering of ferroelectric membranes. *Adv. Mater.* **32**, 2003780 (2020).
29. Marksz, E. J. et al. Broadband, high-frequency permittivity characterization for epitaxial $Ba_{1-x}Sr_xTiO_3$ composition-spread thin films. *Phys. Rev. Appl.* **15**, 064061 (2021).
30. Gao, W. et al. Flexible $PbZr_{0.52}Ti_{0.48}O_3$ capacitors with giant piezoelectric response and dielectric tunability. *Adv. Electron. Mater.* **3**, 1600542 (2017).
31. Pan, H. et al. Defect-induced, ferroelectric-like switching and adjustable dielectric tunability in antiferroelectrics. *Adv. Mater.* **35**, 2300257 (2023).
32. Hao, L. et al. Achieving a high dielectric tunability in strain-engineered tetragonal $K_{0.5}Na_{0.5}NbO_3$ films. *Npj Comput. Mater.* **7**, 62 (2021).
33. Goud, J. P. et al. Thickness dependence of microwave dielectric tunability in $Ba_{0.5}Sr_{0.5}TiO_3$ thin films deposited by pulsed laser deposition. *Ceram. Int.* **49**, 1188–1194 (2023).
34. Crunteanu, A. et al. Characterization and performance analysis of BST-based ferroelectric varactors in the millimeter-wave domain. *Crystals* **11**, 277 (2021).
35. Dawley, N. M. et al. Targeted chemical pressure yields tuneable millimetre-wave dielectric. *Nat. Mater.* **19**, 176–181 (2020).
36. Abdulazhanov, S. et al. THz thin film varactor based on integrated ferroelectric $HfZrO_2$. *ACS Appl. Electron. Mater.* **5**, 189–195 (2023).
37. Aspe, B. et al. Frequency-tunable slot-loop antenna based on KNN ferroelectric interdigitated varactors. *IEEE Antennas Wirel. Propag. Lett.* **20**, 1414–1418 (2021).
38. Mao, F. et al. Ultra-tunable dielectric capacitors enhanced by coupling ferroelectric field effect and semiconductor field effect. *Appl. Phys. Lett.* **125**, 223502 (2024).
39. Gong, F.-H. et al. Absence of critical thickness for polar skyrmions with breaking the Kittel's law. *Nat. Commun.* **14**, 3376 (2023).
40. Damodaran, A. R. et al. Three-state ferroelastic switching and large electromechanical responses in $PbTiO_3$ thin films. *Adv. Mater.* **29**, 1702069 (2017).
41. Platten, S. F. et al. Twinning microstructure in the solid-phase epitaxial crystallization of $BaTiO_3$. *APL Mater* **11**, 081121 (2023).
42. Liu, R. et al. Optical and electronic functionality arising from controlled defect formation in nanoscale complex oxide lateral epitaxy. *Sci. Adv.* **10**, eadk5509 (2024).
43. Wang, A., Chen, R., Yun, Y., Xu, J. & Zhang, J. Review of ferroelectric materials and devices toward ultralow voltage operation. *Adv. Funct. Mater.* **35**, 2412332 (2025).
44. Yang, J. & Liu, S. Topological phase transitions in perovskite superlattices driven by temperature, electric field, and doping. *Phys. Rev. B* **110**, 214112 (2024).
45. Li, W. et al. Delineating complex ferroelectric domain structures via second harmonic generation spectral imaging. *J. Materiomics* **9**, 395–402 (2023).
46. Cherifi-Hertel, S. et al. Shedding light on non-Ising polar domain walls: Insight from second harmonic generation microscopy and polarimetry analysis. *J. Appl. Phys.* **129**, 081101 (2021).
47. Dai, C. et al. Strain effects on stability of topological ferroelectric polar configurations in $(PbTiO_3)_n/(SrTiO_3)_n$ superlattices. *Appl. Phys. Lett.* **123**, 052903 (2023).
48. Cole, K. S. & Cole, R. H. Dispersion and absorption in dielectrics I. Alternating current characteristics. *J. Chem. Phys.* **9**, 341–351 (1941).
49. Cole, K. S. & Cole, R. H. Dispersion and absorption in dielectrics II. Direct current characteristics. *J. Chem. Phys.* **10**, 98–105 (1942).
50. Rijal, S., Nahas, Y., Prokhorenko, S. & Bellaiche, L. Dynamics of polar vortex crystallization. *Phys. Rev. Lett.* **133**, 096801 (2024).
51. Johnson, K. M. Variation of dielectric constant with voltage in ferroelectrics and its application to parametric devices. *J. Appl. Phys.* **33**, 2826–2831 (1962).
52. Fu, Z. & Xu, Y. Microstructure and dielectric tunable properties of $Ba_{0.5}Sr_{0.5}TiO_3$-$Li_2Zn_3Ti_4O_{12}$ composite ceramics. *Ceram. Int.* **50**, 1248–1253 (2024).
53. Ruan, H. et al. Microwave characterization of two $Ba_{0.6}Sr_{0.4}TiO_3$ dielectric thin films with out-of-plane and in-plane electrode structures. *J. Adv. Ceram.* **12**, 1521–1532 (2023).
54. Huo, C. et al. Robust tunability and newly emerged Q resonance of $Ba_{0.8}Sr_{0.2}TiO_3$-based microwave capacitors under Gamma irradiations. *ACS Appl. Mater. Interfaces* **16**, 23517–23524 (2024).
55. De Backer, A., van den Bos, K. H. W., Van den Broek, W., Sijbers, J. & Van Aert, S. StatSTEM: An efficient approach for accurate and precise model-based quantification of atomic resolution electron microscopy images. *Ultramicroscopy* **171**, 104–116 (2016).
56. Hatab, Z., Gadringer, M. E. & Bösch, W. Propagation of linear uncertainties through multiline Thru-Reflect-Line calibration. *IEEE Trans. Instrum. Meas.* **72**, 1007409 (2023).
57. Wu, J., Yang, J., Ma, L., Zhang, L. & Liu, S. Modular development of deep potential for complex solid solutions. *Phys. Rev. B* **107**, 144102 (2023).
58. Hu, Y., Yang, J. & Liu, S. Giant piezoelectric effects of topological structures in stretched ferroelectric membranes. *Phys. Rev. Lett.* **133**, 046802 (2024).
59. Plimpton, S. Fast parallel algorithms for short-range molecular dynamics. *J. Comput. Phys.* **117**, 1–19 (1995).
60. Kresse, G. & Furthmüller, J. Efficient iterative schemes for ab initio total-energy calculations using a plane-wave basis set. *Phys. Rev. B* **54**, 11169–11186 (1996).
61. Kresse, G. & Furthmüller, J. Efficiency of ab-initio total energy calculations for metals and semiconductors using a plane-wave basis set. *Comput. Mater. Sci.* **6**, 15–50 (1996).
62. Perdew, J. P. et al. Restoring the density-gradient expansion for exchange in solids and surfaces. *Phys. Rev. Lett.* **100**, 136406 (2008).
63. Gu, Z. et al. Resonant domain-wall-enhanced tunable microwave ferroelectrics. *Nature* **560**, 622 (2018).

64. Meyers, C. J. G., Freeze, C. R., Stemmer, S. & York, R. A. (Ba,Sr)TiO_3 tunable capacitors with RF commutation quality factors exceeding 6000. *Appl. Phys. Lett.* **109**, 112902 (2016).
65. Yang, L. et al. Microwave properties of epitaxial (111)-oriented $Ba_{0.6}Sr_{0.4}TiO_3$ thin films on Al_2O_3 (0001) up to 40 GHz. *Appl. Phys. Lett.* **97**, 162909 (2010).
66. Ahmed, A., Goldthorpe, I. A. & Khandani, A. K. Electrically tunable materials for microwave applications. *Appl. Phys. Rev.* **2**, 011302 (2015).

Acknowledgements

This work was financially supported by the Basic Science Center Project of National Natural Science Foundation of China (NSFC) under Grant No. 52388201 (QL, J.-F. L.), NSFC grants No. U24A2009 (QL), 12474087 (QL), and 52172268 (QZ), Ministry of Education of China Scientific Research Innovation Capability Support Project for Young Faculty under Grant No. ZYGXQNJSKYCXNLZCXM-M17 (QL), National Key Basic Research Program of China under Grant No. 2020YFA0309100 (QL) and by Beijing Municipal Natural Science Foundation under Grant No. JQ24011 (QL) and Z240008 (QL). The computational resource is provided by Westlake HPC Center and supported by the Open-Source Supercomputing Center of S.-A.-I. J.Y. and S.L. acknowledge the support from Zhejiang Provincial Natural Science Foundation of China (LR25A040004). Work performed at the Center for Nanoscale Materials and Advanced Photon Source, both U.S. Department of Energy Office of Science User Facilities, was supported by the U.S. DOE, Office of Basic Energy Sciences, under Contract No. DE-AC02-06CH11357.

Author contributions

Q.L. conceived and designed the project. S.W. and Y.M. performed film growth and electrical measurements. J.Y. and S.L. performed MD simulations. H.G. and Q.Z. performed STEM imaging. K.O. and H.F. performed in-situ synchrotron XRD. R.L., T.Z., and M.H. performed X-ray nano-imaging. J.-F.L. discussed the results. S.W. and Q.L. wrote the manuscript with input from all the authors.

Competing interests

The authors declare no competing interests.

Additional information

Supplementary information The online version contains supplementary material available at https://doi.org/10.1038/s41467-026-69440-x.

Correspondence and requests for materials should be addressed to Shi Liu or Qian Li.

Peer review information *Nature Communications* thanks the anonymous reviewers for their contribution to the peer review of this work. A peer review file is available.